



Intense Vortex Motion in a Two-Phase Bioreactor

Bulat R. Sharifullin¹, Sergey G. Skripkin¹, Igor V. Naumov^{1,*}, Zhigang Zuo^{2,*}, Bo Li³
and Vladimir N. Shtern^{1,4}

¹ Laboratory of Heat and Mass Transfer Problems, Kutateladze Institute of Thermophysics, Siberian Branch of the Russian Academy of Sciences, 1 Academician Lavrent'ev Avenue, 630090 Novosibirsk, Russia

² State Key Laboratory of Hydrosience and Engineering, Department of Energy and Power Engineering, Tsinghua University, Beijing 100084, China

³ Beijing Key Laboratory of Information Service Engineering, Beijing Union University, Beijing 100101, China

⁴ Shtern Research and Consulting, Houston, TX 77096, USA

* Correspondence: naumov@itp.nsc.ru (I.V.N.); zhigang200@tsinghua.edu.cn (Z.Z.)

Abstract: The paper reports the results of experimental and numerical studies of vortex motion in an industrial-scale glass bioreactor (volume, 8.5 L; reactor vessel diameter D , 190 mm) filled 50–80%. The model culture medium was a 65% aqueous glycerol solution with the density $\rho_g = 1150 \text{ kg/m}^3$ and kinematic viscosity $\nu_g = 15 \text{ mm}^2/\text{s}$. The methods of particle image velocimetry and adaptive track visualization allow one to observe and measure the vortex motion of the culture medium. In this work, the vortex flow investigation was performed in a practical bioreactor at the operation regimes. Our research determines not only the optimal flow structure, but also the optimal activator rotation speed, which is especially important in the opaque biological culture. The main result is that, similar to the case of two rotating immiscible liquids, a strongly swirling jet is formed near the axis, and the entire flow acquires the pattern of a miniature gas–liquid tornado. The aerating gas interacts with the liquid only through the free surface, without any mixing. This intensifies the interphase mass transfer due to the high-speed motion of the aerating gas.

Keywords: vortex reactor; complex vortex; vortex flow modeling; phase boundary; immiscible liquids; free surface



Citation: Sharifullin, B.R.; Skripkin, S.G.; Naumov, I.V.; Zuo, Z.; Li, B.; Shtern, V.N. Intense Vortex Motion in a Two-Phase Bioreactor. *Water* **2023**, *15*, 94. <https://doi.org/10.3390/w15010094>

Academic Editors: Maksim Pakhomov and Pavel Lobanov

Received: 27 November 2022

Revised: 22 December 2022

Accepted: 23 December 2022

Published: 28 December 2022



Copyright: © 2022 by the authors. Licensee MDPI, Basel, Switzerland. This article is an open access article distributed under the terms and conditions of the Creative Commons Attribution (CC BY) license (<https://creativecommons.org/licenses/by/4.0/>).

1. Introduction

The evolution of fluid mechanics has been driven by the connection between science and the practical needs throughout history, from the hydromechanics of “the ancients” through the Newtonian era and up to the present day. It is safe to say that vortex motion is one of the fundamental states of a liquid medium [1,2]. According to the vivid expression provided in the Saffman’s book [3], vortices are “sinews and muscles of fluid motion”.

Although the existence of vortices of various types has been known for a long time [3], diverse metamorphoses of vortex formation and vortex transfer of mass and energy require deeper analysis and understanding [4–6]. An important and interesting fact that needs additional interpretation is the formation of vortex motion during the interaction between various liquid and gaseous media (e.g., a gas vortex in an aqueous medium [7,8] and slippage in flows containing nanoparticles [9]) or immiscible liquid media differing both in density and viscosity [10].

In technical applications, vortex mixing is a widespread method of mass transfer enhancement. In vortex combustion chambers, vortex cells stabilize the flame and reduce harmful emissions. In chemical gas and biological two-liquid reactors, the organization of vortex motion contributes to mixing of ingredients, thus increasing the yield of the net product [4]. A convenient model of a vortex reactor is a vertical cylindrical container, where movement of the filling liquid is generated through an intermediate liquid or a gaseous medium by rotating one of the end disks [4–6]. Notably, in the case of a single-component

liquid, it is not that important which of the end disks is rotating; for the case of using two media or a free boundary, it is possible to compensate for the influence of gravity on the shape of the interface between the immiscible components by choosing the size of the inductor generating a vortex structure [11]. Naumov et al. [12] reported a similarity in the patterns of formation and evolution of the recirculation zones in the center and on the free end of an intensely swirled flow generated in a non-uniformly filled cylinder due to the opposite end rotation. The flow topology appears to be independent of properties of the medium (liquid or gas) at the free boundary, thus limiting fluid circulation and location of the disk generating the vortex structure [13,14].

Many vortex devices allow for interaction between a rotating working fluid and a layer of another liquid or air (e.g., when the reactor is partially filled with the working fluid). Recently, researchers have focused on two-fluid rotating flows in the context of developing vortex-aerated bioreactors. In searching for an optimal flow shape for culture growth in vortex bioreactors, an interesting and impressive structure has been discovered: it simulates strong vortices observed in the atmosphere and ocean and can be called “a two-story tornado” [15]. It has been revealed that the tornado-like flow develops in bioreactors as well.

The bioreactor is the main component in industrial-scale microbiological synthesis [16]. Microbial cells can withstand vigorous stirring and aeration. Animal and plant cells are more fragile and sensitive to mechanical action regardless of the cultivation method (in suspension or in an immobilized state). The aim of using the bioreactor is to provide optimal conditions for the growth of cultivated biological objects and biosynthesis of the target product while maintaining the sterility and cost-effectiveness of the process. During deep aerobic biosynthesis, the bioreactor contains a system of components, which are a suspension of cells (or other aforementioned cultures) in a nutrient medium enriched with dissolved oxygen. The system requires the maintenance of certain conditions—heat and mass transfer—as well as aeration of the medium.

The technological complexity of ensuring the parameters of the mixing process for different types of cells and microorganisms explains the wide variety of designs of industrial bioreactors. On the basis of the principle of operation, traditional bioreactors are included in one of the following four groups: (a) bubbling and airlift bioreactors, where mixing is realized due to the air flow supplied through the medium; (b) bioreactors with a mechanical “stirrer” in the mixed medium; (c) combinations of the first two types; and (d) highly specialized and unique ones, created for one process.

Leaving behind the conventional devices, we explain the characteristics of the gas vortex bioreactor using a fundamentally new mixing method employing a concentrated air vortex generated by an activator installed under the bioreactor lid above the surface of the culture medium. Mixing of the culture medium is carried out by creating a three-dimensional motion of the “rotating vortex ring” type: a quasi-stationary flow with an axial counterflow generated by an aerating gas vortex due to the pressure drop above the surface and the friction force of the air flow on the liquid surface.

The absence of a mechanical stirring element in the liquid ensures energy saving (0.06–0.1 W/L, compared to 1–4 W/L for bioreactors with a mechanical stirring device and airlift bioreactors), soft and efficient mixing of liquids—including viscous ones—without foam formation, cavitation (surface aeration without using a bubbler—for cell cultures), hydraulic shocks, highly turbulent or stagnant zones, and micro zones with high temperature [16].

In contrast to previous studies, here we explore the vortex flow in a real-world bioreactor. The aim of this work is to identify the regularities of vortex flow in an aerial vortex bioreactor at various activator rotation parameters. Knowing the rotation parameters, it is possible to determine the flow mode in any opaque culture medium. The culture is placed in a liquid that is activated by an upper medium (air) driven by the rotation of the activator. Therefore, it is responsible not only the optimal flow structure, but also for the optimal rotation speed, thus ensuring soft and thorough mixing of ingredients and preventing them from directly contacting the activator. The biological culture is not destroyed because it

does not contact the rotating solid parts of the reactor. Meanwhile, the effective mixing and saturation of the working medium with nutrients and oxygen is ensured.

2. Materials and Methods

2.1. Experimental Setup

The patterns of vortex motion were studied in an industrial-scale GV FBR 10-I glass cylindrical bioreactor manufactured by the Center for Vortex Technologies (volume, 8.5 L; diameter of the reactor vessel $D = 190$ mm; and height $H = 300$ mm) (Figure 1a). A 65% aqueous glycerol solution was used as a model liquid (density $\rho_g = 1150$ kg/m³; kinematic viscosity $\nu_g = 15$ mm²/s). In the reactor, mixing of the cell suspension was carried out by creating a quasi-stationary rotational motion generated by a swirling gas flow. The tornado-like swirling gas flow was generated by an impeller (activator) above the surface of the culture medium (Figure 1b). The aerating gas interacted with the cell suspension only through the free surface of the latter, without mixing with it. As a result, the interfacial mass transfer was intensified due to the high velocity of the aeration gas, and the suspension was mixed evenly, without stagnant zones.

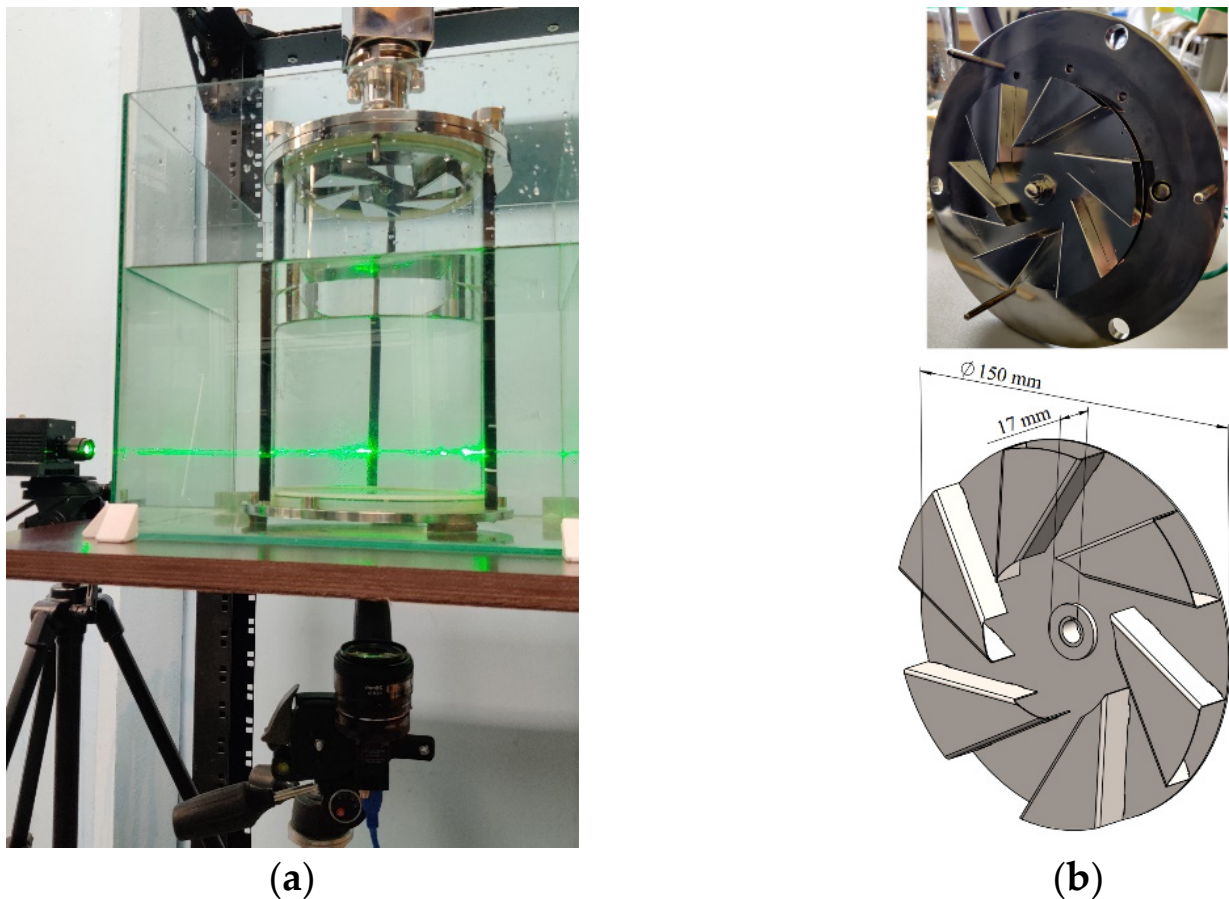


Figure 1. (a) A gas–liquid bioreactor: a photo of the test bench; (b) an impeller (activator) generating vortex motion in the bioreactor.

Due to the interface friction and pressure difference between the periphery and the center of the gas vortex, such a swirl of the aerating gas ensures the movement of the model liquid in the form of a vortex ring, rotating with respect to the tank axis with simultaneous downward liquid motion at the periphery of the tank and ascending motion in the axial zone [14,15].

Figure 2 shows the organization of vortex motion in a bioreactor and the diagram of the test bench. The gas–vortex reactor was placed in a glass container sized $300 \times 300 \times 400$ mm

to reduce optical aberrations and ensure thermal stabilization. The vortex motion of air was generated by an activator at a rotation speed Ω of up to 1000 rpm at the minimal filling of 50% ($h_g = 150$ mm) and, by continuously adding the working model medium, to the maximal filling of 80% ($h_g = 240$ mm).

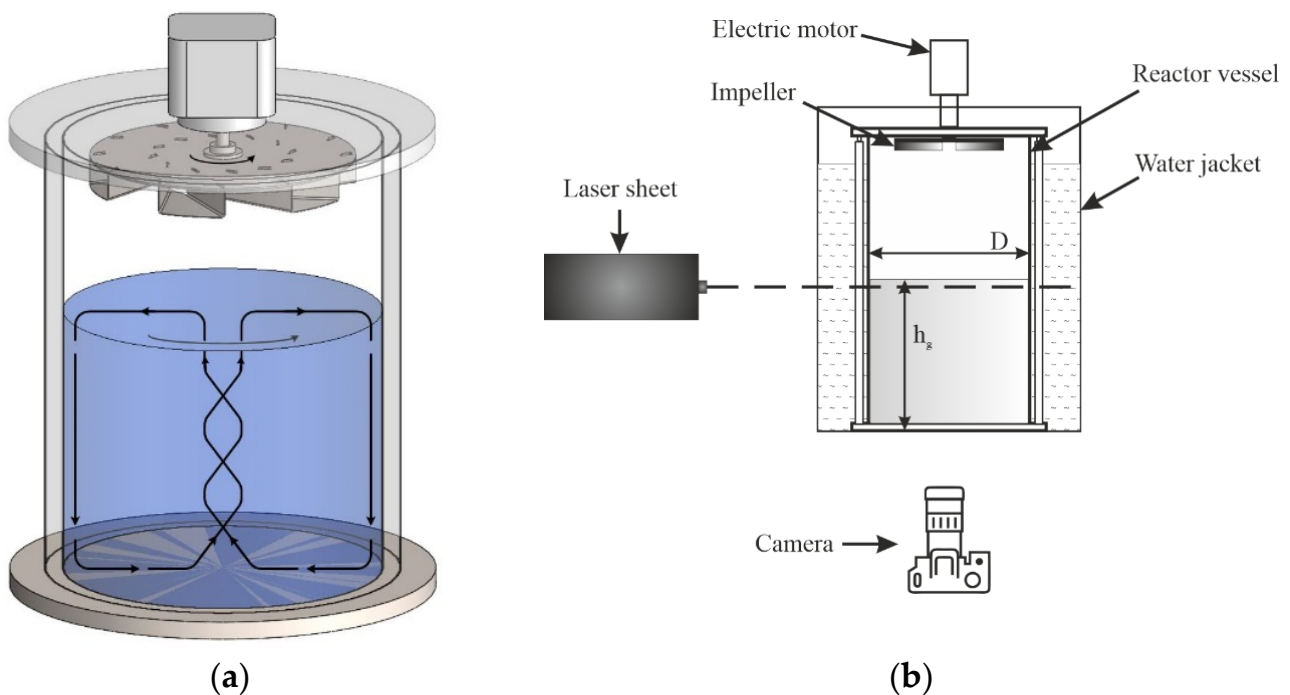


Figure 2. The experimental setup: (a) organization of vortex motion and (b) setup diagram.

The velocity fields were measured by Particle Image Velocimetry (PIV). The PIV method provided an instantaneous velocity distribution in the investigated cross-section and an instantaneous flow pattern within the two-dimensional plane of the light sheet. The PIV and adaptive track visualization methods were used to observe the vortex motion pattern [13,14,17]. Polyamide beads (density, 1030 kg/m^3 ; diameter, $\sim 10 \mu\text{m}$) were employed as seeding light-scattering particles for both flow visualization and PIV measurements. The air flow was seeded by a fog generator. Measurements were performed in a horizontal section in the vicinity of the interface, at a distance of 2 mm in air and liquid and near the bottom of the reactor vessel, as well as in a vertical section passing through the axis of the cylinder. The light cross-section was formed by a laser sheet of the PIV measuring system [14], and the image was recorded by a camera through the transparent glass bottom and sidewall of the bioreactor.

The PIV system consisted of a double-pulsed Nd:YAG Beamtech Vlite-200 laser (wavelength, 532 nm; repetition rate, 15 Hz; pulse duration, 10 ns; pulse energy, 200 mJ), an IMPERX IGV-B2020 CCD camera (8 bits per pixel; matrix resolution 2056×2060 pixels, 1.3" optical format) equipped with a Nikon SIGMA 50 mm f/2.8D lens, and a synchronizing processor. We calculated the two-dimensional velocity fields using the commercial ActualFlow software, Version 1.18.8.0. The thickness of the laser light sheet formed by a cylindrical lens to illuminate tracer particles was ~ 0.8 mm in the measurement plane. The distance between the camera and the laser sheet was 800 mm and 720 mm for the horizontal and vertical planes, respectively.

For every set of experimental conditions, we accumulated 500 images and averaged them to increase the signal-to-noise ratio. Time delay between the two images varied from 5 to 120 ms depending on the fluid type. The velocity fields were calculated using the iterative cross-correlation algorithm with a continuous window shift and deformation and 75% overlap of the interrogation windows in order to have a relatively large dynamic

range (the span between the maximal and minimal velocity values). The threshold value for concentration of seeding particles was 5–8 tracers per 64×64 -pixel area. The sub-pixel interpolation of a cross-correlation peak was performed over three points using one-dimensional approximation by the Gaussian function. The inaccuracy of position determination did not exceed 0.1 pixel. Thus, the velocity measurement–error estimates were 1% and 4% for tracer sizes of 8 and 2 pixels, respectively. The resulting spatial resolution of the velocity fields was approximately one vector per 1.4 mm. A more detailed description of the applied methods of experimental diagnostics and the composition of measuring systems can be found in [13,14,17].

The paper considers the structure of the circulation motion of the working fluid in the mode implying the formation of a laminar soft circulating movement of the working fluid for growing cultures that are not resistant to unfavorable hydrodynamic conditions and require soft mixing. This mode of bubble-free aeration is implemented using an activator: a high-speed gas vortex is formed above the surface and swirls the culture medium, thus creating a weak circulation movement and simultaneously saturating it with oxygen. The optimal operating range of the activator rotation with neither interface fluctuations nor foaming is 180–900 rpm.

2.2. The CFD Approach

Numerical calculations were carried out in order to complete the flow structure in the upper medium (air) where PIV measurements are difficult to perform, especially in the vertical section. The main focus of the calculations was placed on the vortex motion of the air medium generated by the rotating impeller. The numerical simulations were performed using the OpenFOAM software [18,19]. The finite volume method (FVM) was used to solve the incompressible Navier–Stokes equations, and the volume of fluid (VOF) method was adopted for capturing the liquid–gas interface [18–20]. The Multiple Reference Frame (MRF) method was used to calculate the rotating domain. The MRF approach was employed to control volume with multiple zones at different rotational speeds. The fluids (gas and water) were treated as incompressible and immiscible Newtonian fluids where the heat and mass transfer are neglected. The equations of continuity and momentum were solved:

$$\frac{\partial \rho}{\partial t} + \nabla \cdot (\rho U) = 0 \quad (1)$$

$$\frac{\partial(\rho U)}{\partial t} + \nabla \cdot (\rho U U) = -\nabla p + \nabla \cdot s + \rho g + F \quad (2)$$

where $\rho = \alpha \rho_l + (1 - \alpha) \rho_a$; subscripts 'l' and 'a' represent the liquid and gas phases, respectively. F is the source term due to surface tension, which is modeled using the Continuum Surface Force (CSF) method. $s = \mu(\nabla U + \nabla U^T - 2/3(\nabla \cdot U)I)$ is the viscous stress tensor; I is the identity tensor; and $\mu = \alpha \mu_l + (1 - \alpha) \mu_a$ is the dynamic viscosity.

The incompressible Navier–Stokes equation in the relative frame with absolute velocity could be written as [21–23]

$$\begin{aligned} \frac{\partial U_R}{\partial t} + \frac{d\Omega}{dt} \times r + \nabla \cdot (U_R \otimes U_S) + \Omega \times U_S &= -\nabla \left(\frac{p}{\rho}\right) + \nu \nabla \cdot \nabla (U_S) \\ \nabla \cdot U_S &= 0 \end{aligned} \quad (3)$$

where U is the absolute velocity; the subscripts R and S indicate the rotary and stationary components, respectively. Ω is the rotational speed of the reference frame for a stationary observer, which is equal to the rotational speed of the rotor. p and ρ denote the pressure and density, respectively. The density is $\rho_g = 1150 \text{ kg/m}^3$ for glycerol and $\rho_a = 1.2 \text{ kg/m}^3$ for air. The kinematic viscosities are $\nu_g = 15 \text{ mm}^2/\text{s}$ for glycerol and $\nu_a = 18 \text{ mm}^2/\text{s}$ for air; the surface tension is $\sigma = 0.05 \text{ N/m}$.

The NS equations were solved using the Direct Numerical Simulations (DNS). The time ranged from 0 to 10 s. The Courant number was set at 0.1, and the time increment was adjustable. In order to eliminate the prime error, we averaged the results during the last 5 s.

The computational domain and mesh are shown in Figure 3. For simplicity, the rotor shaft was neglected in simulations. The domain diameter was 180 mm, and the height was 250 mm. It contained 364,421 hexahedral grids. The refinement mesh was adopted in the gas domain, as shown in Figure 3. Furthermore, the boundary condition of the enclosed vessel and rotor walls was no-slip. The initial condition for the pressure over the free surface was set at $p_0 = 101,325$ Pa. The gravity was considered here, where $g = 9.8$ m/s².

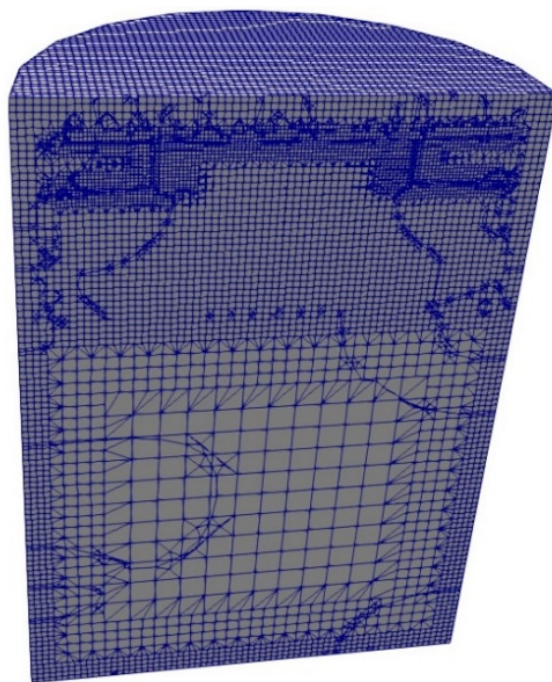


Figure 3. The computational domain and the mesh system.

3. Results

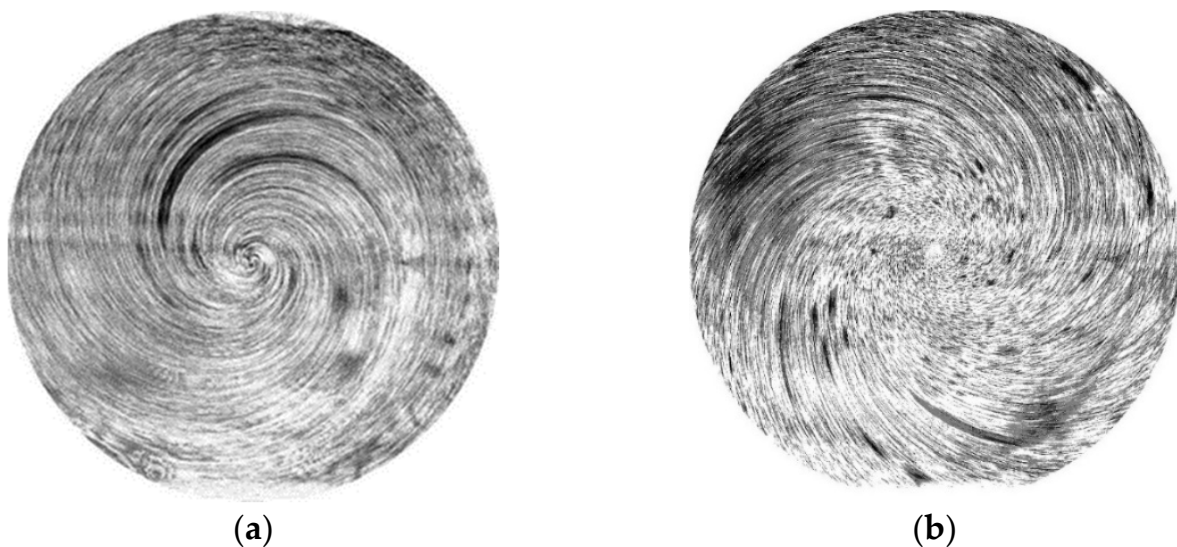
3.1. Experimental

An experimental study of the flow structure was carried out for several stationary modes at $\Omega = 90, 180, 360, 540, 720,$ and 900 rpm using the PIV method and the developed hardware and software of the adaptive track visualization complex. The adaptive visualization method made it possible to qualitatively investigate the flow structure. For the motion formation, there is an analogy with the case of a two-liquid system [10,13], where the lower heavy fraction has a divergent flow under the interface and a converging flow near the bottom. The study was carried out in a horizontal section in the vicinity of the interface and bottom in the liquid at a distance of 2 mm.

Table 1 shows the maximum values of the measured tangential velocity components (V_{tgm}) depending on the velocity of the activator (Ω) at $h = 0.5$ and 0.8 . These values serve to determine the characteristic Re_g . In this case, the Reynolds number for the liquid is defined as $Re_g = V_{tgm}R/\nu_g$, where V_{tgm} is the maximum value of the tangential component of the velocity, R is the radius of the reactor vessel, and ν is the kinematic viscosity of the working fluid. The use of a 2.3 MP sensor Sony IMX174 with 10 Hz framing and a delay of up to 100 ms allowed us to significantly improve quality of the recorded images, and the preliminary subtraction of the background image reduced the noise level. Figure 4 shows examples of converging and diverging helical motion of the working fluid under the interface (Figure 4a) and in the vicinity of the bottom (Figure 4b), which illustrates the circulating meridional movement of the working fluid generated by an intense air vortex in the bioreactor.

Table 1. The maximum values of the tangential velocity under the interface and the Reynolds number in the liquid, depending on the rotation of the activator.

	Ω , rpm	V_{tgm} , mm/s	Re
$h = 0.5$	180	7.7	48.8
	360	18.1	114.6
	540	29.2	184.9
	720	36	228
	900	46.8	296.5
$h = 0.8$	180	9.7	61.3
	360	18.5	117.4
	540	32.4	205.5
	720	52.5	332.7
	900	77.1	488.6

**Figure 4.** Visualization of the motion of the model fluid: (a) the flow diverging from the axis below the interface and (b) the flow converging to the axis near the bottom at $\Omega = 900$ rpm, $h_g = 0.5h$.

The PIV method was used to obtain and analyze the velocity fields and profiles of the azimuthal and radial velocity components in air and in liquid at distances of 2 mm from the interface. Figure 5 shows the streamlines reconstructed from the vector fields obtained in a horizontal section near the interface when the reactor vessel was filled by 50%.

At low Ω , there is a strongly converging flow in the air above the interface, where the centrifugal force acts on the medium adjacent to the swirler and meridional air circulation is observed, like in the case of the two-liquid system. As Ω increases, a turbulent flow is formed in the air near the reactor axis; it appears as a diverging flow near the interface (Figure 4, left column). In the liquid, the processes occur according to the classical scenario of vortex interactions in two-fluid systems [6,24,25]. At low Ω , a centrifugal cell of meridional circulation arises near the axis, thus increasing its intensity with rising Ω . This scenario of vortex development and circulating fluid motion is observed both at 50% and 80% filling of the bioreactor with a model medium.

Figures 6–8 show the profiles of the tangential V_{tg} and radial V_r velocity components in the horizontal section in the vicinity of the interface in air and the model liquid at low and high rotation speeds of the activator $\Omega = 90, 180, 360, 540,$ and 720 rpm. Further, for convenience, the heights of reactor filling with the working fluid $h_g = 210$ mm and 340 mm are presented in dimensionless quantities $h = H/h_g = 0.5$ and $h = H/h_g = 0.8$, respectively.

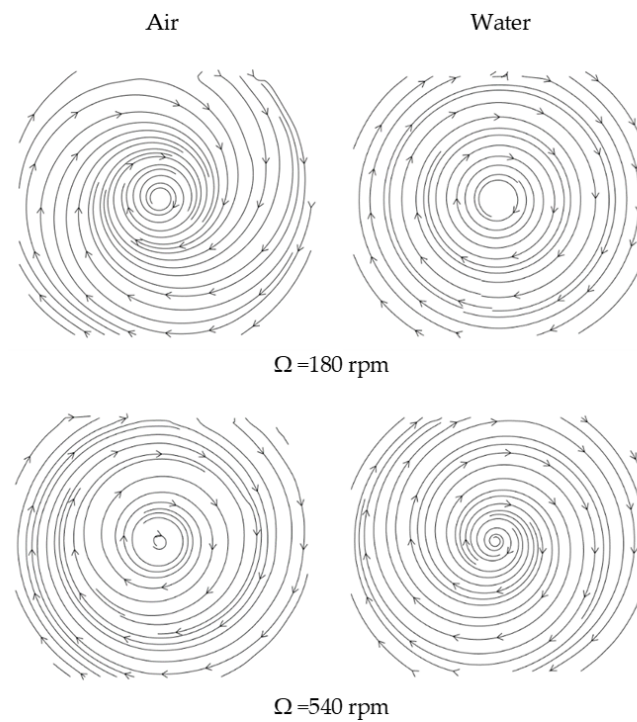


Figure 5. The streamlines reconstructed from the vector fields obtained in a horizontal section near the interface ((left)—in air; (right)—in the working model fluid).

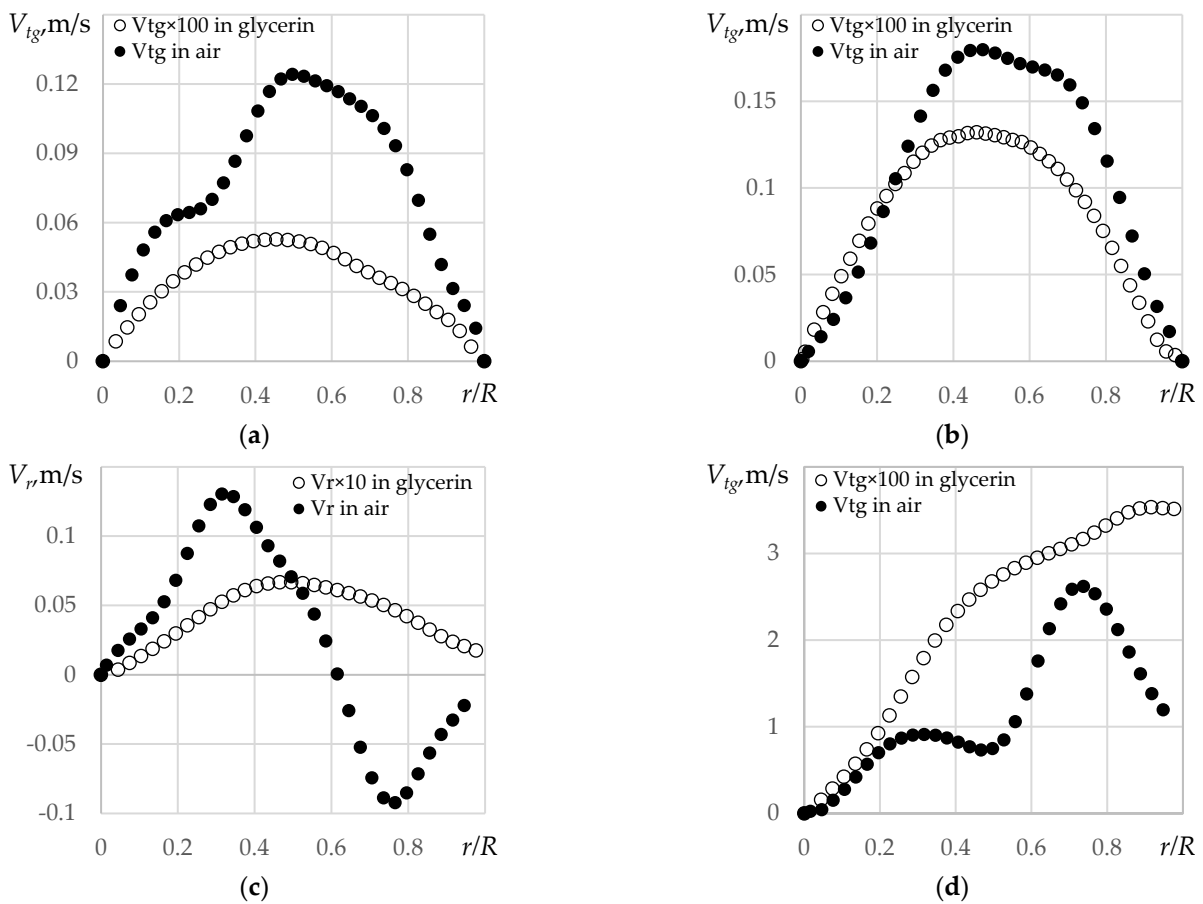


Figure 6. The tangential velocity profiles at $\Omega = 90$ rpm: (a) $h = 0.5$; (b) $h = 0.8$; and (c,d) the radial and tangential velocities at $\Omega = 720$ rpm and $h = 0.5$, respectively.

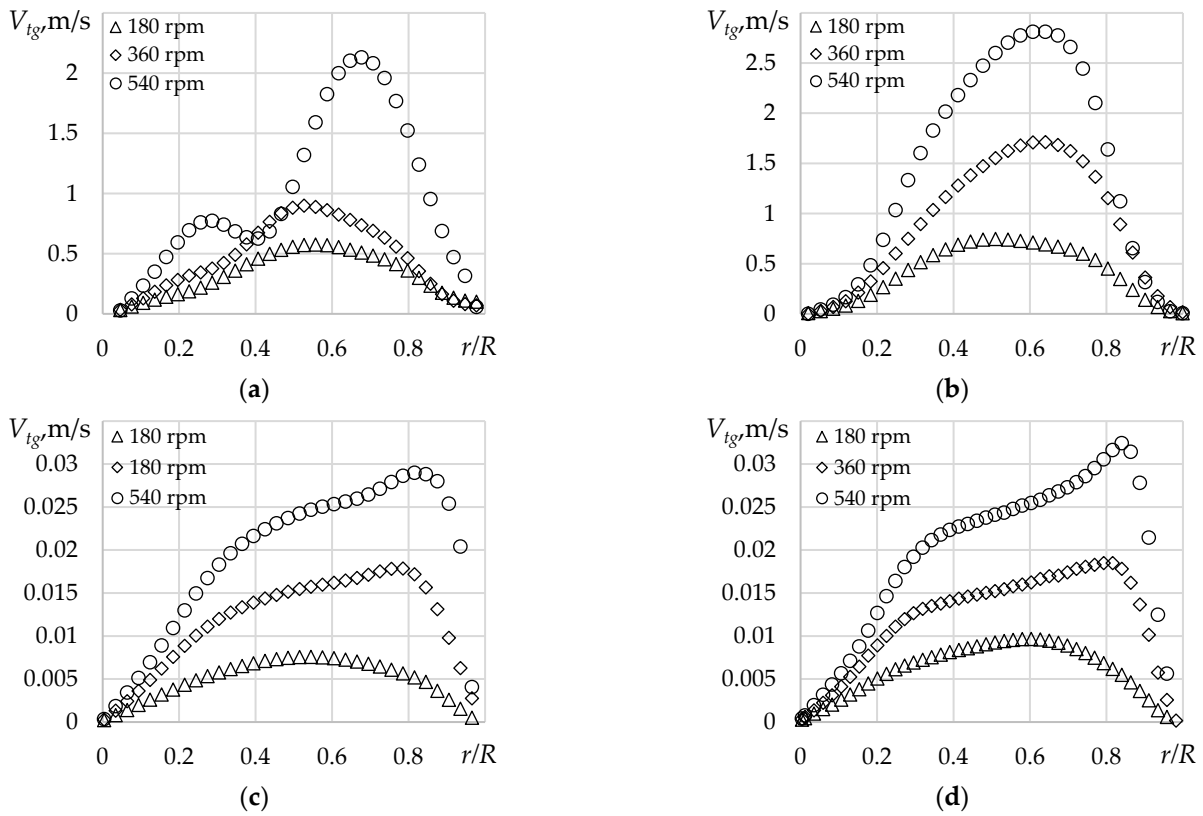


Figure 7. Tangential velocity profiles in air (a) at $h = 0.5$, (b) at $h = 0.8$, and in glycerin (c) at $h = 0.5$ and (d) at $h = 0.8$.

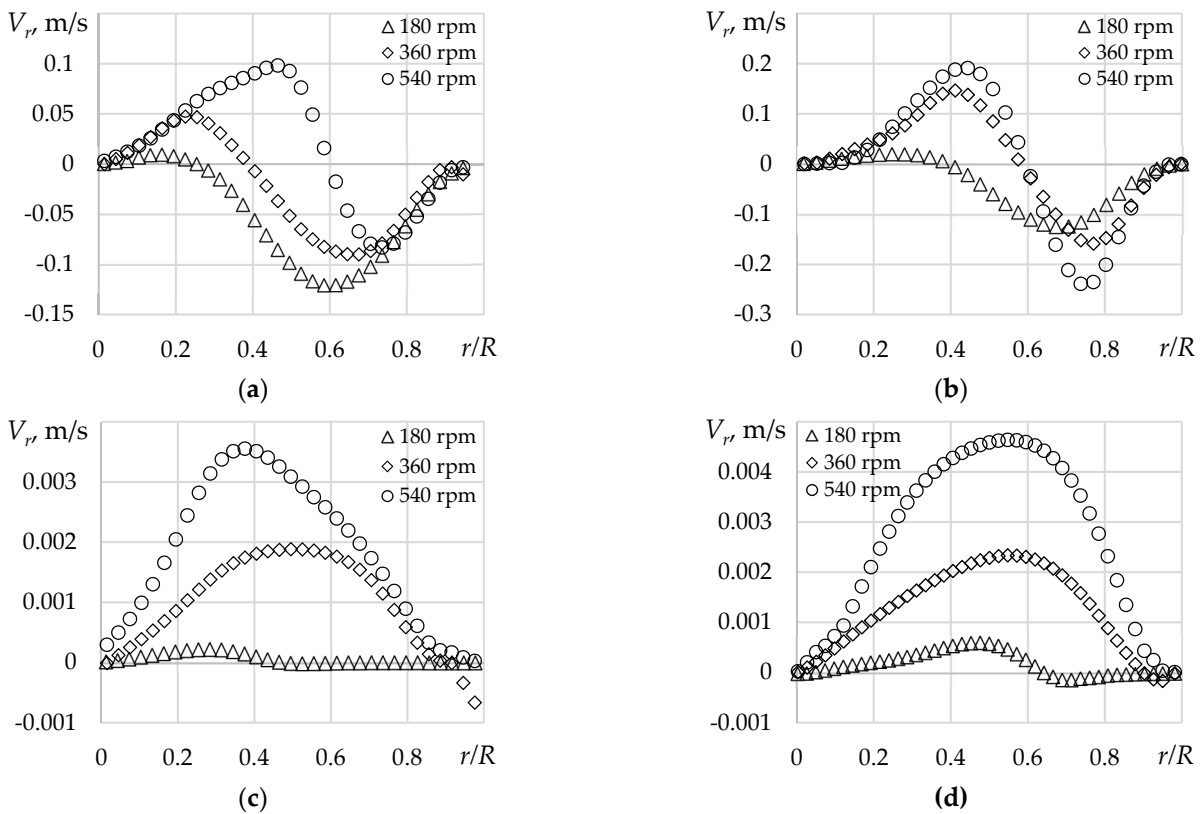


Figure 8. The radial velocity profiles in air (a) at $h = 0.5$, (b) at $h = 0.8$, and in glycerol (c) at $h = 0.5$ and (d) at $h = 0.8$.

Figure 6 compares the profiles of the tangential and radial velocity components in air and liquid at $\Omega = 90$ and 720 rpm. It shows only the tangential velocity profiles for $\Omega = 90$ rpm, since the radial velocity of the fluid in this mode is too low to be measured using the PIV method. Since the maximum tangential velocity in a liquid is two orders of magnitude lower than that in air, for convenience, Figure 6 shows the values of the tangential velocity of the liquid multiplied by 100; Figure 6c presents the values of the radial velocity of the liquid multiplied by 10.

Figure 6 shows that the maximum values of the profiles at $\Omega = 90$ rpm are much smaller than those at $\Omega = 720$ rpm; due to the considerable difference in densities of liquid and air, the velocity profiles differ by one or two orders of magnitude. In order to avoid big differences in the velocity values in the same diagram, the data were grouped by types of the medium, so Figures 7 and 8 show the profiles only for $\Omega = 180, 360,$ and 540 rpm.

Figure 7 shows the tangential component of velocity. Although the maximum velocities in air and in the liquid differ by two orders of magnitude, even with small flow swirls, at $\Omega = 180$ rpm, the vortex motion is generated in the model liquid. As Ω increases to 540 rpm, this trend persists and becomes more pronounced despite the fact that the maximum values still differ by two orders of magnitude. Meanwhile, as it can be seen from Figure 5a, the knee of the tangential velocity component profile increases at $h = 0.5$. Visual observations in the vertical section indicate that a non-stationary vortex appears in the air as Ω on the axis increases, while centrifugal circulation is observed at the periphery: the air flow sinks along the wall to the bottom and rises up about half the radius before reaching the axis. A double vortex is presumably formed in the air: an internal non-stationary vortex and an external toroidal one with centrifugal circulation. This assumption is confirmed by the values of the radial velocity component (Figure 7a,b) at points where the velocity values reverse their sign from positive to negative. Hence, a flow directed towards the periphery appears in the axis region with increasing Ω .

Having compared the values of the tangential velocity component in air and the model liquid, one may note that the trend of angular momentum transfer at small and large flow swirl values, as well as different volumes of the model liquid, is fully maintained. Thus, the results obtained are consistent with the earlier data for liquid vortex systems, where a less dense liquid swirled a denser liquid [24,25]. The characteristic non-stationary processes in air, which manifest themselves, among other things, in the formation of nested vortex cells characterized by changes in circulation and velocity values at which the air–liquid interface does not undergo fluctuations, are not specific for the model liquid.

Figure 8 shows that, at $\Omega = 180$ rpm, the air flow is directed towards the axis (negative velocity values), while divergent motion from the axis to the periphery is already beginning to form in the model fluid, and the values of the radial velocity component are becoming positive. Therefore, the converging vortex air flow forms a divergent motion in the model fluid.

The diagrams in Figure 8c,d demonstrate how the central circulation appears and grows in the model fluid. At $\Omega = 180$ rpm, the radial velocity component in the model fluid is small, while at $\Omega = 540$ rpm, the maximum value of the radial velocity component increases by an order of magnitude to reach values of several millimeters per second. In the meantime, the profiles of both tangential and radial velocity do not have abrupt bends, which indicates that both vortex and meridional motions of the model fluid are formed in the entire volume of the bioreactor.

As it has been shown in an experimental study focusing on the structure of a closed vortex flow of two immiscible liquids [25], there is a similarity in the development of the cellular structure in the cases of the one- and two-liquid systems, and the Reynolds number of the lower liquid is close to that for the one-liquid system. This analogy is also true for the case when the vortex motion in the working medium is formed by a gas vortex.

In order to detect an increase in the circulation cell in the model fluid, the flow structure in a vertical section passing through the cylinder axis was studied at $\Omega = 180, 360, 540, 720,$ and 900 rpm. The velocity fields were obtained and analyzed using the PIV method.

Figure 9 shows the profiles of the axial component of velocity V_{ax} in the liquid on the reactor axis, demonstrating the enlargement of the circulation cell and formation of an upward flow along the cylinder axis at $\Omega = 360, 540, 720,$ and 900 rpm and $h = 0.5$ and 0.8 .

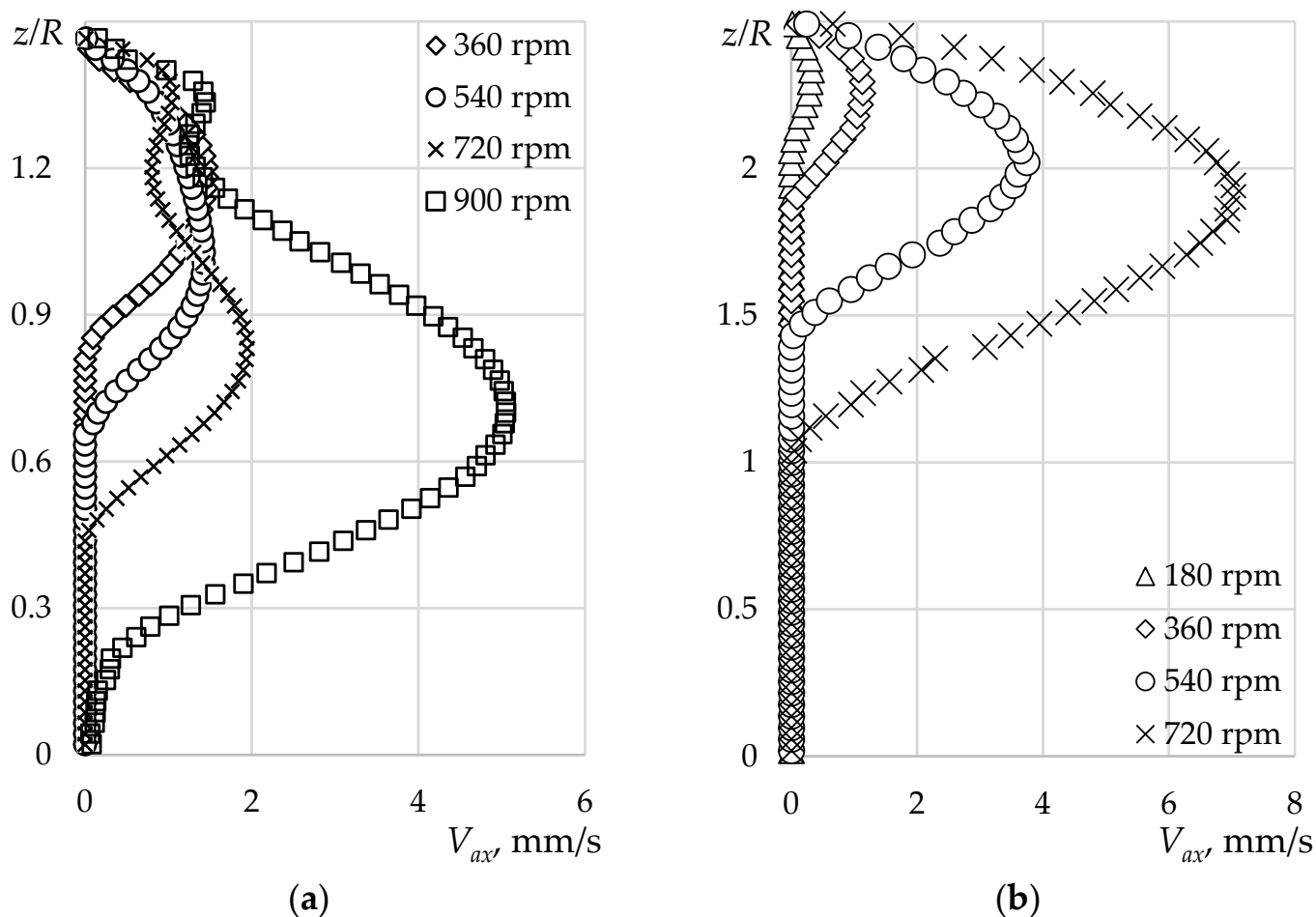


Figure 9. The profiles of the axial velocity component at (a) $h = 0.5$ and (b) 0.8 .

The results presented in Figure 9 show that the development of vortex motion in a gas–vortex bioreactor and propagation of the vortex structure deep into the volume of the working fluid occur concordantly, like in the case of two immiscible liquids [25]. The vortex cell reaches the bottom only at the maximum values of the activator rotation $\Omega = 900$ rpm, which must be taken into account when cultivating viscous media, at $\nu_g > 10$ cCt. When working with low-viscosity media (e.g., when cultivating microalgae in which the solution viscosity is close to that of water), full meridional circulation, according to Table 1 and the results of work [25], will already be achieved at the value of the activator rotation $\Omega > 180$ rpm.

3.2. Numerical Data

The data on the structure of the vortex air flow were obtained using numerical simulations. The numerical calculations were verified by individual velocity profiles and showed acceptable compliance when comparing the velocity profiles over the interface (Figure 10). At high activator rotational speeds, the differences were somewhat greater; nevertheless, the numerical calculations reproduced the main features of the flow, such as the shape of the tangential velocity profile and the change in direction of the radial velocity component.

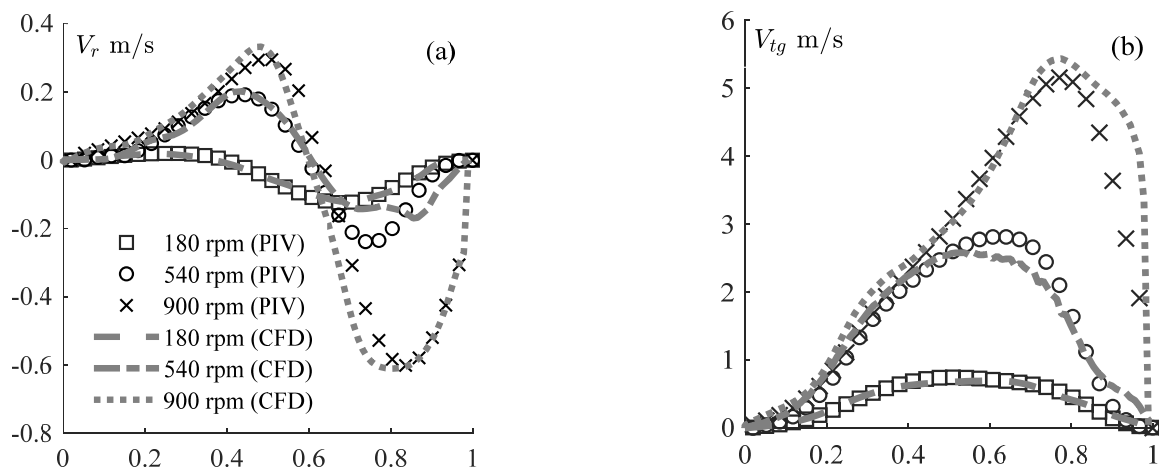


Figure 10. Comparison between the numerical and experimental (a) radial and (b) tangential profiles above the air–water interface at $\Omega = 180, 360, 720,$ and 900 rpm.

Figure 11 shows the numerical simulation data for three different impeller speeds $\Omega = 180, 540,$ and 900 rpm for $h = 0.8$ in the vertical cross-section. The color shows the absolute velocity value, the arrows show the direction of the flow in a vertical cross-section, the white region represent vane. The fields were obtained by time averaging during 5 s. The velocity maximum corresponds to the area near the impeller, and its value depends almost linearly on the rotational speed. The structure of the flow in the upper part of the bioreactor is turbulent and unsteady; the Reynolds numbers in the experiments and calculations lie in the range of 5000–25,000.

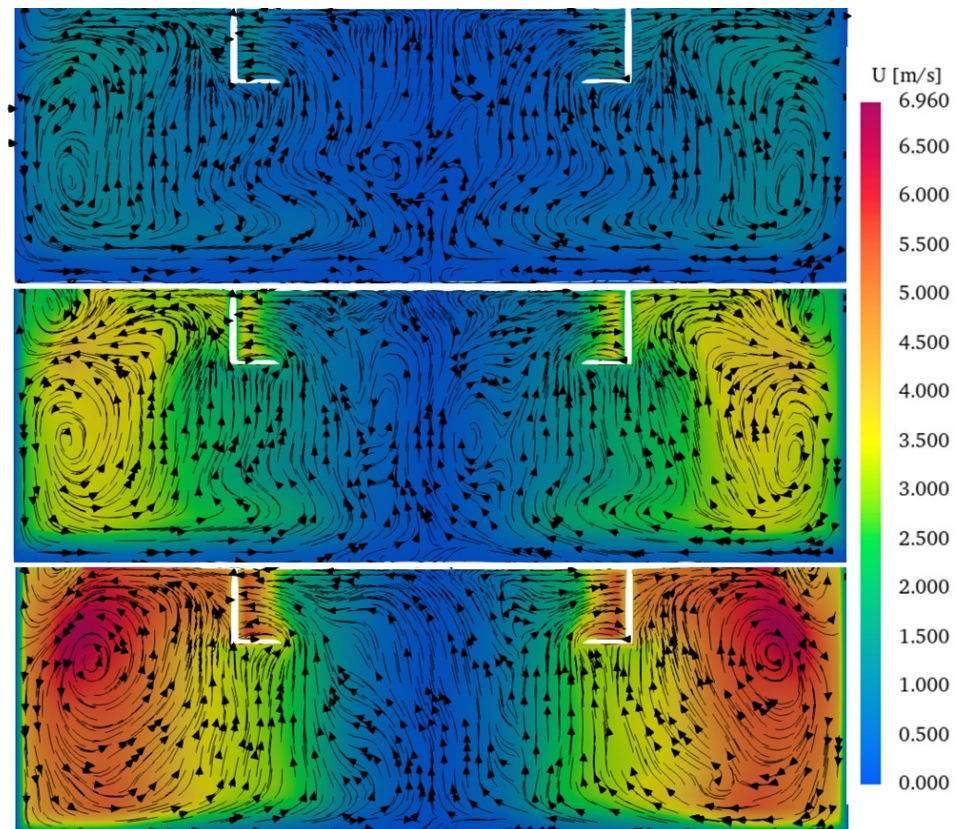


Figure 11. The velocity fields and streamlines in the vertical cross-section: $\Omega = 180$ rpm (top), $\Omega = 540$ rpm (middle), and $\Omega = 900$ rpm (bottom).

In Figure 12, one can see the different slope angle of the streamlines. The arrows show the direction of the flow in a horizontal cross-section. For the $\Omega = 900$ rpm flow regime, the radial velocity component is degenerated, and the central vortex area is formed; in turn, spiral motion towards the center is observed for $\Omega = 180$ rpm, which agrees well with the current lines in Figure 5. The good agreement between the numerical data and the experimental findings allows for the numerical calculations to be used to find the optimal bioreactor filling as well as to investigate important upscaling issues.

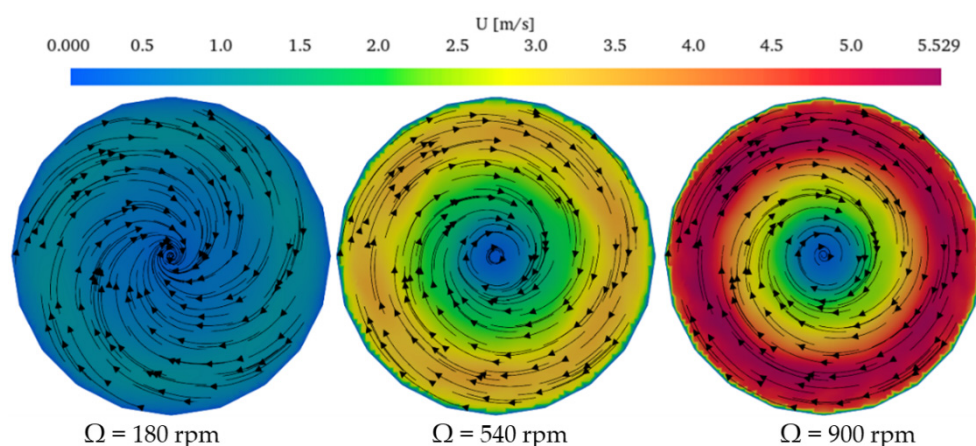


Figure 12. The velocity fields and streamlines are 2 mm above the interface in air.

Both the experimental and numerical results indicate an interesting and paradoxical fact that a spiral flow of a lighter upper media (air) converging above the interface generates a diverging spiral motion of a denser lower fluid (water) under the interface like it occurs in the two-fluid systems [26].

4. Conclusions

This paper reveals and explains the flow structure in a gas–vortex reactor at different flow swirl parameters. We show that there are common features of the vortex motion of the working medium depending on its volume, viscosity, and activator rotation intensity. The main finding is that, similar to the case of two rotating liquids [12,13], a strongly swirled jet is formed at the reactor axis, and the entire flow acquires a structure of a miniature gas–liquid tornado. When the activator rotates, a meridional and circulating flow occurs in the working liquid. Centrifugal circulation cells appear under the interface and increase into the depth of the reactor with increasing speed of the activator rotation. The centrifugal circulation of the working fluid appears similar to that in a closed vortex flow for the one-liquid system, and in the lower liquid, to that in a system of two swirling immiscible liquids [23]. A striking feature is that the radial velocity component slips at the interface, while the air flow descending to the reactor axis forms a divergent vortex motion of the model liquid medium despite the difference in densities being more than three orders of magnitude.

In this study, the vortex flow investigation was performed in a real-world bioreactor at the operation regimes. Our research determined not only the optimal flow structure, but also the optimal activator rotation speed, which is especially important for opaque biological cultures.

Author Contributions: Conceptualization, I.V.N. and V.N.S.; methodology, S.G.S., Z.Z. and B.R.S.; validation, I.V.N., Z.Z. and V.N.S.; formal analysis, I.V.N., V.N.S. and B.R.S.; investigation, B.R.S., Z.Z., B.L. and S.G.S.; writing—original draft preparation, I.V.N., V.N.S. and Z.Z.; writing—review and editing, I.V.N. and Z.Z.; visualization, B.R.S., B.L. and S.G.S.; supervision and project administration, I.V.N.; funding acquisition, I.V.N. All authors have read and agreed to the published version of the manuscript.

Funding: This research was funded by the Russian Science Foundation, grant number 19-19-00083.

Institutional Review Board Statement: Not applicable.

Informed Consent Statement: Not applicable.

Data Availability Statement: Not applicable.

Conflicts of Interest: The authors declare no conflict of interest.

Nomenclature

D	diameter of the reactor vessel
F	source term due to surface tension
g	gravitational acceleration
H	height of the reactor vessel
h_g	height of model fluid
$h = h_g/H$	dimensionless height of model fluid
I	identity tensor
p	pressure
p_0	initial pressure above the free surface
R	radius of the reactor vessel
$Re = V_{tgm}R/v_g$	the Reynolds number
$s = \mu(\nabla U + \nabla U^T - 2/3(\nabla \cdot U))I$	viscous stress tensor
U	absolute velocity
V_{ax}	axial component of velocity
V_r	radial component of velocity
V_{tg}	tangential component of velocity
V_{tgm}	the maximum value of the tangential component of velocity
Subscripts	
a	air
g	aqueous glycerol solution
l	liquid
r	radial component
R	rotary
S	stationary
tg	tangential component
m	maximum value
Greek	
$\mu = \alpha\mu_l + (1 - \alpha)\mu_a$	dynamic viscosity
$\rho = \alpha\rho_l + (1 - \alpha)\rho_a$	density
ρ_a	density of air
ρ_g	density of aqueous glycerol solution
ν_a	kinematic viscosity of air
ν_g	kinematic viscosity of aqueous glycerol solution
Ω	rotation speed of activator
σ	surface tension
Acronym	
CFD	Computational Fluid Dynamics modeling
CSF	Continuum Surface Force method
DNS	Direct Numerical Simulations
FVM	Finite Volume Method
MRF	Multiple Reference Frame method
NS	Navier–Stokes
PIV	Particle Image Velocimetry
VOF	Volume of Fluid method

References

1. Poincaré, H. *Théories des Tourbillons*; George Carre: Paris, France, 1893.
2. Marusic, I.; Broomhall, S. Leonardo da Vinci and Fluid Mechanics. *Annu. Rev. Fluid Mech.* **2021**, *53*, 1–25. [[CrossRef](#)]
3. Saffman, P.G. *Vortex Dynamics*; Cambridge University Press: New York, NY, USA, 1993.
4. Shtern, V. Cellular Flows. In *Topological Metamorphoses in Fluid Mechanics*; Cambridge University Press: New York, NY, USA, 2018.
5. Stepanova, E.V.; Chaplin, T.O.; Chashechkin, Y.D. Experimental investigation of oil transport in a compound vortex. *J. Appl. Mech. Tech. Phy.* **2013**, *54*, 79–86. [[CrossRef](#)]
6. Shtern, V.N.; Naumov, I.V. Swirl-decay mechanism generating counterflows and cells in vortex motion. *J. Eng. Thermophys.* **2021**, *30*, 19–39. [[CrossRef](#)]
7. Byalko, A.V. Underwater gas tornado. *Phys. Scripta* **2013**, *155*, 014030. [[CrossRef](#)]
8. Faugaret, A.; Duguet, Y.; Fraigneau, Y.; Witkowski, L. A simple model for arbitrary pollution effects on rotating free-surface flows. *J. Fluid Mech.* **2022**, *932*, A2. [[CrossRef](#)]
9. Hejazi, H.A.; Khan, M.I.; Raza, A.; Smida, K.; Khan, S.U.; Tlili, I. Inclined surface slip flow of nanoparticles with subject to mixed convection phenomenon: Fractional calculus applications. *J. Indian Chem. Soc.* **2022**, *99*, 100564. [[CrossRef](#)]
10. Naumov, I.V.; Sharifullin, B.R.; Kravtsova, A.Y.; Shtern, V.N. Velocity jumps and the Moffatt eddy in two-fluid swirling flows. *Exp. Therm. Fluid. Sci.* **2020**, *116*, 110116. [[CrossRef](#)]
11. Naumov, I.V.; Chaplina, T.O.; Stepanova, E.V. Investigation of the influence of a vortex flow inductor on the shape of the interface between two immiscible liquids. *Process. Geoenviron.* **2020**, *1*, 599–610. (In Russian)
12. Naumov, I.V.; Kashkarova, M.V.; Okulov, V.L.; Mikkelsen, R.F. The structure of the confined swirling flow under different phase boundary conditions at the fixed end of the cylinder. *Thermophys. Aeromech.* **2020**, *27*, 93–98. [[CrossRef](#)]
13. Naumov, I.V.; Sharifullin, B.R.; Tsoy, M.A.; Shtern, V.N. Dual vortex breakdown in a two-fluid confined flow. *Phys. Fluids* **2020**, *32*, 061706. [[CrossRef](#)]
14. Naumov, I.V.; Skripkin, S.G.; Shtern, V.N. Counter flow slip in a two-fluid whirlpool. *Phys. Fluids* **2021**, *33*, 061705. [[CrossRef](#)]
15. Naumov, I.V.; Gevorgiz, R.G.; Skripkin, S.G.; Sharifullin, B.R. Experimental investigation of vortex structure formation in a gas-vortex bioreactor. *Thermophys. Aeromech.* **2022**, *29*, 719–724.
16. Mertvetsov, N.P.; Ramazanov, Y.A.; Repkov, A.P.; Dudarev, A.N.; Kislykh, V.I. Gas-vortex bioreactors “BIOK”. In *Use in Modern Biotechnology*; Novosibirsk Branch of the Publishing House “Nauka”: Novosibirsk, Russia, 2002. (In Russian)
17. Skripkin, S.G.; Tsoy, M.A.; Naumov, I.V. Visualization the different type of vortex breakdown in conical pipe flow with high cone angle. *J. Flow Vis. Image Process.* **2021**, *28*, 43–53. [[CrossRef](#)]
18. Wu, S.; Li, B.; Zuo, Z.; Liu, S. Dynamics of a single free-settling spherical particle driven by a laser-induced bubble near a rigid boundary. *Phys. Rev. Fluids* **2021**, *6*, 093602. [[CrossRef](#)]
19. Wang, Z.; Liu, S.; Li, B.; Zuo, Z.; Pan, Z. Large cavitation bubbles in the tube with a conical-frustum shaped closed end during a transient process. *Phys. Fluids* **2022**, *34*, 063312. [[CrossRef](#)]
20. Zeng, Q.; An, H.; Ohl, C.D. Wall shear stress from jetting cavitation bubbles: Influence of the stand-off distance and liquid viscosity. *J. Fluid. Mech.* **2022**, *932*, A14. [[CrossRef](#)]
21. Siddiqui, M.S.; Rasheed, A.; Tabib, M.; Kvamsdal, T. Numerical investigation of modeling frameworks and geometric approximations on NREL 5MW wind turbine. *Renew. Energ.* **2019**, *132*, 1058–1075. [[CrossRef](#)]
22. Mizzi, K.; Demirel, Y.K.; Banks, C.; Turan, O.; Kaklis, P.; Atlar, M. Design optimisation of Propeller Boss Cap Fins for enhanced propeller performance. *Appl. Ocean Res.* **2017**, *62*, 210–222. [[CrossRef](#)]
23. Helal, M.M.; Ahmed, T.M.; Banawan, A.A.; Kotb, M.A. Numerical prediction of sheet cavitation on marine propellers using CFD simulation with transition-sensitive turbulence model. *Alex. Eng. J.* **2018**, *57*, 3805–3815. [[CrossRef](#)]
24. Naumov, I.V.; Sharifullin, B.R.; Shtern, V.N. Vortex breakdown in the lower fluid of a two-fluid swirling flow. *Phys. Fluids* **2020**, *32*, 014101. [[CrossRef](#)]
25. Sharifullin, B.R.; Naumov, I.V. Angular momentum transfer across the interface of two immiscible liquids. *Thermophys. Aeromech.* **2021**, *28*, 67–78. [[CrossRef](#)]
26. Naumov, I.V.; Sharifullin, B.R.; Skripkin, S.G.; Tsoy, M.A.; Shtern, V.N. A Two-Story Tornado in a Lab. In *Processes in GeoMedia—Volume V*; Chaplina, T., Ed.; Springer: Cham, Germany, 2022; pp. 25–34.

Disclaimer/Publisher’s Note: The statements, opinions and data contained in all publications are solely those of the individual author(s) and contributor(s) and not of MDPI and/or the editor(s). MDPI and/or the editor(s) disclaim responsibility for any injury to people or property resulting from any ideas, methods, instructions or products referred to in the content.